Numerical Modeling of a Wave Turbine and Estimation of Shaft Work

Ravichandra R. Jagannath
Graduate Research Assistant
School of Aeronautics and Astronautics, Purdue University
701 W. Stadium Avenue, West Lafayette, Indiana-47907
rjagann@purdue.edu

Sally P. M. Bane
Assistant Professor
School of Aeronautics and Astronautics, Purdue University
701 W. Stadium Avenue, West Lafayette, Indiana-47907
sbane@purdue.edu

M. Razi Nalim
Professor, Department of Mechanical Engineering
Indiana University Purdue University Indianapolis
723 W. Michigan St., Indianapolis. IN 46202-5160
mnalim@iupui.edu

ABSTRACT

Wave rotors are periodic-flow devices that provide dynamic pressure exchange and efficient energy transfer through internal pressure waves generated due to fast opening and closing of ports. Wave turbines are wave rotors with curved channels that can produce shaft work through change of angular momentum from inlet to exit. In the present work, conservation equations with averaging in the transverse directions are derived for wave turbines, and quasi-one-dimensional model for axial-channel non-steady flow is extended to account for blade curvature effects. The importance of inlet incidence is explained and the duct angle is optimized to minimize incidence loss for a particular boundary condition. Two different techniques are presented for estimating the work transfer between the gas and rotor due to flow turning, based on conservation of angular momentum and of energy. The use of two different methods to estimate the shaft work provides confidence in reporting of work output and confirms internal

---

This is the author's manuscript of the article published in final edited form as:

Jagannath, R. R., Bane, S. P. M., & Razi Nalim, M. (2018). Numerical Modeling of a Wave Turbine and Estimation of Shaft Work. Journal of Fluids Engineering, 140(10), 101106-101106–101113. https://doi.org/10.1115/1.4040015

consistency of the model while it awaits experimental data for validation. The extended wave turbine model is used to simulate the flow in a three-port wave rotor. The work output is calculated for blades with varying curvature, including the straight axial channel as a reference case. The dimensional shaft work is reported for the idealized situation where all loss generating mechanisms except flow incidence are absent, thus excluding leakage, heat transfer, friction, port opening time and windage losses. The model developed in the current work can be used to determine the optimal wave turbine designs for experimental investment.

1. INTRODUCTION

Oscillatory and pulsatile flows are ubiquitous in nature, and the potential for using unsteady flows in a wide range of engineering applications has long been recognized. One of the earliest uses of pulsatile flow was during the World War II in the making of the German V-1 Flying "Buzz" Bomb. The V-1 used a pulsejet engine with a resonant design that maintained cyclic jet discharge, filling, and firing without ignition. However, the potential of unsteady flow devices has largely been neglected due to the substantive improvements in conceptually simple semi-static devices, steady-flow devices or crypto-steady devices, e.g. turbomachines[1]. Understanding and exploiting such unsteady flows would enable significant improvement of engines and thermodynamic cycles for various applications.

Shock tubes and pulsed combustors (including pulse detonation engines) are well-known examples of unsteady-flow devices. A less well-known example is the wave rotor, a technology that has shown unique capabilities to enhance the performance and operating characteristics of a variety of engines and machinery utilizing thermodynamic

cycles. Wave rotors utilize non-steady but periodic flow in multiple channels or passages to generate internal pressure waves that can perform efficient energy transfer. Due to their mechanical simplicity, self-cooling, and fast time response, wave rotors can be used in a wide range of applications. An additional benefit is the production of shaft work due to flow turning in non-axial wave rotor channels, which can be used to power other devices, for example a fan or compressor in a gas turbine engine.

In general, a wave rotor consists of a row of shrouded blades (forming a set of channels) mounted on a rotating drum. A stationary plate at each end of the drum closely seals the channels except for port openings for inflow and outflow of channel gases to and from corresponding stator ducts. The number of ports per cycle of operation depends on the application; for example, a three-port wave divider has one inflow and two outflow ports, a three-port joiner cycle has two inflow and one outflow port, and a four-port pressure-exchange wave rotor has two inflow and two outflow ports. As the drum rotates, the gas in the channels is exposed to these ports in turn. The instantaneous opening of a port to a channel initiates a pressure wave that draws the gas into the rotor through an inflow port or pushes the gas out through an outflow port. In addition, the pressure differential between the port and the channel either drives a shock wave that compresses the gas in the channel or an expansion fan that expands the gas in the channel, and the end walls cause wave reflections that further change the pressure. A well-designed wave rotor operating at design speed is theoretically highly energy efficient due the fact that energy exchange occurs through precisely timed waves instead of mechanical components; however, the complex gas dynamics present

some challenges for optimized design and practical use with predictable performance. For example, flow separation can occur at the channel inlet and across curved blades in the case of non-axial channels, but the effect can be mitigated by optimized design of the inlet duct and limiting curvature. Another potential issue is controlling thermal expansion and cooling of wave rotor channels. At typical operating conditions, the cycling frequency is high and channel walls reach a predictable equilibrium temperature distribution that is constant and moderate relative to peak gas temperature. This allows thermal management and clearance control to accommodate heating and expansion effects. In spite of the practical challenges, the efficient pressure and energy exchange along with simultaneous shaft work production set the wave rotors apart from standard turbomachinery.

The wave rotor concept originated around 1928 with the filing of a patent in Germany to use a wave rotor as a dynamic pressure exchange device[2]. The Brown Boveri Corporation (BBC) implemented the wave rotor in locomotive gas turbines and diesel engine superchargers. The most successful commercial implementation of wave rotors was the Comprex®, a supercharger developed by BBC used in Mazda diesel engine cars[3]. The wave rotor 'superheater' high-enthalpy high-Mach wind tunnel made by Cornell Aero Labs was useful in testing spacecraft models for atmosphere re-entry. In the mid-1950s, the Ruston-Hornsby turbine company designed a wave rotor with helical channels to provide a turbine effect and generate internal shaft work. The rotor was tested over a wide range of operating conditions and was reported to produce 35 hp of shaft work. Later, General Power Corporation developed a pressure-exchange

wave turbine for Ford Motor Company[4]. A thorough review of the history of wave rotor development and application is given in Reference[1].

Over the past 25 years, there has been renewed interest and research on wave rotors using progressively more advanced manufacturing and modeling capabilities[5–8]. In the 1980s Mathur et. al. developed a first order finite difference scheme to perform wave rotor cycle analysis[9]. In the early 1990s, significant progress on wave rotor development, both computationally and experimentally, was made by researchers at NASA GRC. A quasi-1d (Q1d) numerical model was developed to simulate the flow in axial-channel wave rotors[10]. The model includes multiple ports on each end with subsonic or supersonic inflow and outflow, partially open channels and inflow that is incident on the channel at a non-zero angle. Subsequent versions of the model included source terms to account for end-gap leakage, wall friction, heat transfer, turbulent eddy diffusion, fuel stratification and internal combustion[11]. Due to limited computational resources available at the time, most of the wave rotor simulations have been quasi-1d. A limited number of 2-D simulations were conducted[12]. Detailed simulation of wave rotor cycles in multi-dimensions is even now computationally expensive, time-consuming, and requires the use of multiple processors. Therefore, a quasi-1d simulation with empirical or semi-analytical models to capture effects of turbulence, heat transfer, friction, mass leakage, flow incidence, and partially open end effects was developed, allowing for efficient simulation of multiple cases with varying wave rotor geometry.

The model has been validated over a wide range of operating conditions by NASA GRC[13] and Nalim et. al[8] as shown on Figure 1. The model development was complemented by experimental efforts at both NASA GRC and Purdue University. A wave rotor with a three-port flow-divider cycle was developed at NASA for investigation of fundamental wave rotor physics and for calibration of the Q1d model for different loss mechanisms such as port opening time, friction, leakage and heat transfer[14]. With accurate calibration of such losses, the model can then be adapted to simulate any wave rotor with arbitrary port configurations. The three-port cycle acts as a flow divider where a certain fraction of the incoming flow undergoes compression to leave the rotor at a high pressure while the remaining flow undergoes expansion to leave the rotor at a low pressure. The internal gas dynamics of a three-port wave rotor are illustrated in Figure 2. The wave rotor can also be designed as a reacting flow device, resulting in pre-compression, mechanically confined constant-volume combustion and expansion in a single device. Nalim and co-workers have studied internal combustion wave rotors extensively through both computational and experimental work[8, 15–27].

The previous experimental and numerical work on wave rotor development focused on characterizing the wave processes that result in pressure exchange and on internal combustion, and therefore mostly concentrated on axial channels. As discussed earlier, a second major advantage of the wave rotor is the production of shaft work when curved channels are used, but little work has been done on developing or simulating such wave turbines. Experimental testing of multiple wave turbines with varying blade and stator duct geometries can be extremely costly. Therefore, the development of the

numerical model is critical for efficient analysis of loss mechanisms, investigation of the wave dynamics for designing optimal port timings, and testing with a range of blade shapes, duct angles, and boundary conditions. The model can then be used to determine the optimal wave turbine designs for experimental investment.

In the current work, the Q1d numerical model was extended to account for blade curvature and the equations were modified to use the same numerical integration scheme as the axial flow model. A model to estimate losses due to flow incidence at the channel inlet[11] was also implemented. Then, a methodology for estimating the shaft work due to flow incidence and flow turning along the blades was developed. Finally, the extended model and the methodology for estimating shaft work was used to simulate a three-port divider cycle with axial and curved channels. The three-port divider cycle is chosen as a first test case due to the extensive prior studies on this cycle performed at NASA, and also because it provides a case with both compression and expansion in a single device. The model is first used to simulate the three-port cycle with axial channels and the inlet duct design is determined to minimize incidence loss and incidence torque. The optimal inlet duct angle calculated for the axial channel is then incremented or decremented in subsequent simulations for curved channels to arrive at an optimal duct design for the non-axial channel. The shaft work is then estimated for the curved channel case, with minimal incidence torque.

2. NUMERICAL MODEL

The available quasi-1d numerical model for wave rotors was limited to axial channels. Following prior work at NASA GRC[28,29], the conservation equations are re-derived and implemented in the model to allow for blade curvature. A model for incidence loss at the wave rotor inlet[11] is also implemented. Finally, two methods for estimating shaft work are developed based on conservation of energy and of angular momentum.

2.1 Conservation Equations for a Wave Turbine

In this section, the re-formulation of the conservation equations to account for blade curvature is presented. First, the original model equations developed for axial channels are discussed, followed by derivation of the passage-averaged equations for non-axial channels. Finally, the passaged-averaged equations are algebraically manipulated so they can be solved using the numerical scheme developed for axial flow.

2.1.1 Conservation Equations for Axial Channel Wave Rotors

The conservation equations used in the quasi-1d code for axial channels with variable axial cross-section A(x) and constant mean radius are given by[18]:

$$\frac{\partial}{\partial t'}\begin{bmatrix} \rho' A_c' \\ \rho' A_c' u' \\ \dfrac{A_c' p'}{\gamma(\gamma-1)} + \dfrac{\rho' A_c' u'^2}{2} \end{bmatrix} + \frac{\partial}{\partial x'}\begin{bmatrix} \rho' A_c' u' \\ \dfrac{\rho' A_c' u'^2}{2} + \dfrac{p' A_c'}{\gamma} \\ A_c' \left(\dfrac{p'}{\gamma-1} + \dfrac{\rho' u'^2}{2} \right) u' \end{bmatrix} = \psi \tag{1}$$

where the prime notation denotes a non-dimensional variable. The current work is focused on non-reacting flow, therefore the conservation equations for chemical species are not included here but are given in[18]. In general, the source vector Ψ includes contributions from two categories of loss mechanisms: 1) friction, heat transfer to the walls and turbulent eddy diffusion effects throughout the length of the channel, and 2) radial and circumferential leakage only at the two ends of the channel[17]. A third category of loss mechanisms, which include end-region flow separation during periods of partial (gradual) opening of channels and due to flow incidence, are built into the application of boundary conditions, and thus not included in the source term. In the present work, we neglect the first and second category of losses that is provided for in the source vector Ψ, in order to verify energy and angular momentum balance in treating the main effect of blade curvature.

2.1.2 Conservation Equations for Non-Axial Channel Wave Rotors

The conservation equations in (1) cannot be used for non-axial channels because they do not include blade forces and fluctuations along the spanwise and pitchwise directions which arise due to suction and pressure along the top and bottom surfaces of the blade. To account for these effects, the conservation equations for a channel of arbitrary curvature in the tangential and radial directions are averaged over the channel cross-section to reduce the number of spatial variables to one, hence reducing the three-dimensional equations to quasi-1d equations. The averaging of the

governing equations is presented in detail by Welch et. al.[28], and the final channel averaged equations (not including loss source terms) [29]are given by:

$$\frac{\partial}{\partial t}\begin{bmatrix} \overline{\rho} A_c \\ \overline{\rho} A_c \overline{\overline{u_x}} \delta^2 \\ \overline{\rho} A_c \overline{\overline{e_I}} \end{bmatrix} + \frac{\partial}{\partial x}\begin{bmatrix} \overline{\rho} A_c \overline{\overline{u_x}} \\ \overline{\rho} A_c \overline{\overline{u_x}}^2 \delta^2 + \overline{p} A_c \\ \overline{\rho} A_c \overline{\overline{h_I}} \overline{\overline{u_x}} \end{bmatrix} = \begin{bmatrix} 0 \\ F_B + F_C \\ Q_C \end{bmatrix} \quad (2)$$

The overbar in the governing equations denotes an unweighted passage average and the double overbar denotes a density-weighted passage average[29]. The geometries for slanted and curved channels are illustrated in Figure 3 and Figure 4, respectively. The momentum equation involves axial, radial and tangential components, where the tangential and radial velocity components are written in terms of the axial component. This leaves a blockage term in the momentum equation. In general, the blockage term is a function of the blade angle and meridional angle and is written as $\delta^2 = 1 + \overline{\tan\zeta^2} + \overline{\tan\phi^2}$ [29]. The angle ζ is the local blade angle measured in the plane tangent to the axial-azimuthal (x-θ) surface, relative to the rotor axial direction (x), and the angle ϕ is the meridional angle measured in the plane tangent to the axial-radial (x-r) surface, relative to the rotor axial direction (x). As shown in Figure 4, ζ is measured with respect to the rightward horizontal, with counter-clockwise taken to be positive. The blade angle is constant for the slanted or "staggered" straight blade case and varies along the axial direction for the curved blade case.

The source terms F_B and F_c represent blade forces and momentum correlation terms, respectively, and Q_C represents heat flux correlation[28]; note that these terms are separate from the source terms in Ψ due to friction and heat transfer between the

gas and the channel walls. The momentum source term F_c and heat flux term Q_c contain the correlation terms obtained from averaging the three-dimensional gas momentum and energy equations which are non-zero when there are spanwise and pitchwise flow-field variations due to entropy gradients, local acceleration and wave refraction. However, in the one-dimensional model these terms can be neglected without obscuring the basic physics of the problem[29].

The momentum source term F_B is due to the blade force, which is important when there is change in angular momentum due to flow turning. The source term can be expressed in terms of pressure $(\overline{\mathrm{p}})$, area $(\mathrm{A_c})$ and blade angle[29]:

$$\mathrm{F_B} = \frac{\overline{\rho}\left(\overline{\overline{\mathrm{u_x}}}\right)\left(\overline{\overline{\mathrm{u_x}}}\right)\mathrm{A_c}}{2}\frac{\partial\delta^2}{\partial \mathrm{x}} + \overline{\mathrm{p}}\mathrm{A_c}\left[\frac{\Delta_\theta(\tan(\zeta))}{\overline{\overline{\mathrm{R}}}(\theta_\mathrm{P}-\theta_\mathrm{S})} + \frac{\Delta_\mathrm{r}(\tan(\phi))}{(\mathrm{R_T}-\mathrm{R_H})}\right] \tag{3}$$

2.1.3 Simplified Equations for Non-Axial Channel Wave Rotors

To solve the equations as written in (2), the entire numerical scheme used for an axial flow wave rotor would need to be altered as the equations in (2) are substantially different from the equations in (1) for axial flow. In the current work, the passage-averaged equations are manipulated algebraically such that the additional terms from blade curvature in the momentum equation are moved to the source vector and the left hand side of the equation becomes identical to (1). This will allow the model to retain the numerical scheme used for axial channels by simply adding extra terms to the source vector in the code.

The first step involves expressing the change in blade angle (ζ) and meridional angle (ϕ) in terms of the change in cross-sectional area along the axial direction, reducing Eq. (3) to the simpler form:

$$F_B = \frac{\overline{\rho}\left(\overline{\overline{u_x}}\right)\left(\overline{\overline{u_x}}\right)A_c}{2}\frac{\partial \delta^2}{\partial x} + \overline{p}\frac{\partial A_c}{\partial x} \tag{4}$$

The averaged pressure in the momentum equation can be written in terms of the axial velocity component and rotational speed as

$$\overline{p} = (\gamma - 1)\overline{\rho}\left(\overline{\overline{e_I}} - \frac{\left(\overline{\overline{u_x}}\right)\left(\overline{\overline{u_x}}\right)\delta^2}{2} + \frac{\left(\overline{\overline{R\Omega}}^2\right)}{2}\right) \tag{5}$$

where the local specific rothalpy is given by

$$\overline{\overline{h_I}} = \overline{\overline{e_I}} + \frac{\overline{p}}{\overline{\rho}} \tag{6}$$

Substituting Eq. (3-6) into Eq. (2) and normalizing using reference conditions for pressure (P/P^*), temperature (T/T^*), velocity (V/V^*), density (ρ/ρ^*), area (A/L^{*2}) and rotational speed ($\Omega L^*/a^*$). The reference velocity is the speed of sound at a reference temperature of 300K. The reference length is the length of the channel which is 31 inches and the reference pressure is 101325 Pa. The conservation equations can be written in the simplified form

$$\frac{\partial}{\partial t'}[w] + \frac{\partial}{\partial x'}[f(w)] = \chi + \psi \tag{7}$$

$$w = \begin{bmatrix} \rho' {A_c}' \\ \rho' {A_c}' {u_x}' \delta^2 \\ \rho' {A_c}' \left[\dfrac{p'}{(\gamma - 1)\gamma\rho'} + \dfrac{u_x'^2 \delta^2}{2} - \dfrac{R'\Omega'^2}{2} \right] \end{bmatrix}$$

$$f(w) = \begin{bmatrix} \rho' {A_c}' {u_x}' \\ \rho' {A_c}' u_x'^2 \delta^2 + \dfrac{\overline{p}' {A_c}'}{\gamma} \\ \overline{\rho} {A_c}' \left[\dfrac{p'}{(\gamma - 1)\rho'} + \dfrac{u_x'^2 \delta^2}{2} - \dfrac{R'\Omega'^2}{2} \right] u_x' \end{bmatrix}$$

$$\chi = \begin{bmatrix} 0 \\ \dfrac{\rho' u_x'^{\,2} {A_c}'}{2} \left(\dfrac{\partial}{\partial x'} \delta^2 \right) + p' \left(\dfrac{\partial {A_c}'}{\partial x'} \right) \left(\dfrac{1}{\gamma} \right) \\ 0 \end{bmatrix}$$

Once again, the use of prime variables in Eq. (7) indicates non-dimensional quantities and should not be confused with fluctuation terms used in turbulence models. The reference conditions for normalizing the different variables are obtained at ambient conditions of 14.7 psi and 520° Rankine. It is assumed that the channels have a constant mean radius about which the hub and tip shroud are symmetric, the mean meridional angle is zero ($\tan \phi = 0$), and the blockage term can be written as $\delta^2 = 1 + \overline{\tan \zeta^2}$. When the rotor wheel speed Mach number is low, due to gradual opening of the channel to the port, there is flow distortion at the fluid contact interface which is moving behind the shock. At very high Mach numbers, there is radial distortion of this fluid contact interface due to the centripetal effect. An intermediate wheel speed Mach number is chosen so that both the gradual opening time effect and the centripetal effect can be minimized[30]. Therefore, the assumption of neglecting radial distortion is

reasonable. For perfectly axial channels, $\tan\zeta = 0$ and $\delta^2 = 1$, thus reducing the governing equations to the classical quasi-1d equations in (1).

The equations in (7) have additional terms in the momentum and energy equations as a result of the blade force due to flow turning and therefore could be difficult to implement in the original numerical scheme used to solve the equations for the axial flow case. To address this issue, the additional terms can be moved to the right-hand side of the momentum and energy equations through careful algebraic manipulations that account for how the equations are coupled. The terms are then combined with the source vector, leaving the left-hand side of the equations identical to (1), so that the numerical integration scheme used for axial channels can be used without change in the quasi-one-dimensional code. The final form of the conservation equations with new definitions of the variables w, $f(w)$, and χ, obtained after the algebraic manipulations described above is given by:

$$\frac{\partial}{\partial t'}[w] + \frac{\partial}{\partial x'}[f(w)] = \chi + \psi \tag{8}$$

$$w = \begin{bmatrix} \overline{\rho'}\mathrm{A_c}' \\ \overline{\rho'}\mathrm{A_c}'\overline{\overline{u_x'}} \\ \overline{\rho'}\mathrm{A_c}'\left[\dfrac{\overline{p'}}{(\gamma-1)\gamma\overline{\rho'}} + \dfrac{\left(\overline{\overline{u_x'}}\right)\left(\overline{\overline{u_x'}}\right)}{2}\right] \end{bmatrix} \quad f(w) = \begin{bmatrix} \overline{\rho'}\mathrm{A_c}'\overline{\overline{u_x'}} \\ \left(\overline{\rho'}\mathrm{A_c}'\overline{\overline{u_x'}}^2 + \dfrac{\overline{p'}\mathrm{A_c}'}{\gamma}\right) \\ \overline{\rho'}\mathrm{A_c}'\left[\dfrac{\overline{p'}}{(\gamma-1)\overline{\rho'}} + \dfrac{\left(\overline{\overline{u_x'}}\right)\left(\overline{\overline{u_x'}}\right)}{2}\right]\overline{\overline{u_x'}} \end{bmatrix}$$

$$\chi = \begin{bmatrix} 0 \\ \frac{1}{1+\tan^2(\zeta)} \frac{-\rho' \left(\overline{\overline{u_x'}}\right)\left(\overline{\overline{u_x'}}\right) \mathrm{A_c}'}{2} \frac{\partial(1+\tan^2(\zeta))}{\partial x'} + \frac{\overline{p'}}{\gamma} \frac{\partial \mathrm{A_c}'}{\partial x'} + \frac{1}{1+\tan^2(\zeta)} \frac{\mathrm{A_c}' \tan^2(\zeta)}{\gamma} \frac{\partial}{\partial x'}(\overline{p'}) \\ -\overline{\rho'} \mathrm{A_c}' \overline{\overline{u_x'}} \frac{\partial}{\partial x'} \left[\frac{\left(\overline{\overline{u_x'}}\right)\left(\overline{\overline{u_x'}}\right) \tan^2(\zeta)}{2} - \frac{(\overline{\overline{R'\Omega'}}^2))}{2} \right] - \overline{\rho'} \mathrm{A_c}' \frac{\partial}{\partial t} \left[\frac{\left(\overline{\overline{u_x'}}\right)\left(\overline{\overline{u_x'}}\right) \tan^2(\zeta)}{2} - \frac{(\overline{\overline{R'\Omega'}}^2))}{2} \right] \end{bmatrix}$$

The terms due to blade curvature have been moved to the right hand side as part of the source vector and the left-hand side is identical to that of Equation (1). The modified blade-force source vector χ is added to a modified loss source vector ψ to produce an overall source term vector. The contributions due to mass leakage, wall shear stress and heat transfer are not considered in this work; thus, the modified source vector ψ is not described here. Eq. (8) represents the general quasi-1d model for a wave turbine with curved blades of arbitrary profile.

The numerical model presented in this work is a single passage model and quasi-1d. It may not be able to capture the strong gasdynamic interaction between the rotor and port flow fields which is multidimensional. The incidence loss at the inflow plane is solved using a model that treats the incidence separation as a converging diverging nozzle. This is highly simplified, and does not consider that the separation bubble may extend a significant length into the channel. The blade force model developed in this work ignores some of the correlation terms that arise from averaging the conservation equations. The validity of ignoring these terms will need to analyzed by including these terms and modeling them appropriately. Even with these modeling assumptions, the Q1d solver has been shown to predict the wave rotor performance with reasonable accuracy[13]. In addition, the Q1d model has correlations for its source terms that have

been calibrated with previous experiments and therefore provide confidence in prediction with respect to experimental results, although not used in the present work. It is recognized that the incidence loss model requires improvement, possibly with the use of multidimensional transient modeling of small scale separation phenomena that will be substantially more expensive than the current model.

2.1.4 Numerical Integration Scheme

This conservation equations for curved channels given in (9) are solved in a manner similar to the equations for an axial channel wave rotor using an explicit second-order Lax-Wendroff total-variation-diminishing (TVD) scheme with Roe's flux-averaging technique to capture discontinuities. A total of 200 computational cells are used for the current work, which provides a non-dimensional computational cell size of 0.005. A short study was conducted to verify that the results are independent of cell size (for grid sizes of 200 cells and larger), details are given in Section 3. The non-dimensional time step was set to 0.001 to maintain a Courant number of 0.2 for numerical stability of the model.

In prior work by NASA GRC, Eq. (2) and (3) were used in their model. This would mean the numerical integration scheme developed for axial channel had to be changed to account for additional terms due to blade curvature. In the current work, Eq. (2) and (3) were modified to Eq. (8) and solved using the same numerical scheme as axial channels. The modified equations for a wave turbine were verified against numerical predictions from NASA GRC[29] for the specific case of an expansion wave originating at one end of a non-axial channel, traveling through the length of the channel and

reflecting at the end wall[19]. The results confirmed that in a non-axial channel the arrival of the wave after reflection from the end wall is delayed, consistent with the increased length of travel for the wave. Therefore, the port timing should be optimized for the specific geometry of the channel, including its length. For a straight, slanted channel, the gas axial velocity was verified to be proportional to the cosine of the blade angle, consistent with the wave strength for a given expansion pressure ratio. Further verification was also performed by setting the blade angle ζ to zero and verifying that the axial channel results could be reproduced.

2.2 Incidence Loss at the Wave Rotor Inlet

The gas flow into the rotor channel in the channel frame of reference is rarely aligned and most often enters at an angle with respect to the channel, called the relative frame inflow angle, i. The flow incidence leads to stagnation pressure loss at the inlet and flow separation may form a vena contracta as illustrated in Figure 5. As the flow turns to align with the channel direction it generates an incidence torque. In the case of a non-axial channel wave rotor, it is important to distinguish between torque contributions from incidence and from blade curvature. Since incidence results in total pressure loss, it is usually desirable to design the inlet duct to minimize the contribution due to incidence, i.e. minimize the relative-frame inflow angle. However, incidence can usually be minimized only on average over a given port and for a given operating condition, since the channel inlet velocity typically varies over the port and its distribution changes with operating conditions. In the current work, the relative frame inflow angle is estimated as:

$$\mathrm{i} = \tan^{-1}\left(\frac{\vec{c}\sin(\beta) + \overrightarrow{\Omega \mathrm{R}}}{u}\right) - \zeta_l \tag{9}$$

and the optimal duct angle is achieved when the relative frame inflow angle is zero in an average sense.

The incidence turning is implemented in the wave rotor model by treating the vena contracta created by the flow separation bubble as a backward-facing step[11] occurring within a negligibly short distance from the inlet plane. The inlet stagnation pressure, stagnation temperature, and duct angle are provided as input boundary conditions, with the initial conditions in the first computational cell also known, while the flow velocity entering the channel from the inlet duct both in the channel frame of reference and stationary frame of reference are unknown. An initial guess is made for the static pressure in the duct and used in two ways to calculate the velocity entering the first cell after flow re-attachment in the channel. First, the velocity is found using conservation of mass, momentum and energy (entropy generation), by assuming isentropic nozzle flow from the inlet stagnations conditions to wall-parallel flow at the step, followed by reattachment. The height of the vena contracta and the downstream velocity is obtained based on whether or not the nozzle is choked. Second, the initial guess for the static pressure is used to calculate the velocity into the first computational cell using Roe's approximate-Riemann flux-averaging method, similar to the method used to calculate the velocity between the interior cells in the channel. Any difference between the two values of velocity requires correction of the initially assumed static pressure by iteration until the two velocities are equal. Details of the method are given

in Ref. [11]. The flow conditions determined through this iterative process are then used for the flow in the duct. Using the calculated flow conditions, the duct angle, and the rotational speed, the flow velocity in the stationary frame of reference and relative frame inflow angle, i can be calculated. The incidence torque and the rotor torque can be calculated using the flow conditions at the wave rotor inlet and exit using the methodology described in the following section.

2.3 Shaft Work Estimation

The gas undergoes changes in angular momentum due to flow incidence at the inlet as well as flow turning along the curved surface of the channel, resulting in work being transferred into or out of the gas to satisfy conservation of angular momentum. The gas also does work on the blades leading to a change in the stagnation enthalpy. If the system, consisting of a wave rotor blade channel in this case, is considered to be adiabatic with no heat transfer through its walls then the change in stagnation enthalpy must be equal to the work being transferred into or out of the gas to satisfy conservation of energy. Therefore, work transfer estimated through conservation of energy and conservation of angular momentum should be equal. Note that although the flow within the wave rotor is non-steady, it is periodic and so there is no net accumulation of angular momentum or energy over a complete cycle. Comparing the work transfer calculated using the two different methods provides an internal consistency check in the modeling, while validation of the model itself awaits experimental research.

2.3.1 Shaft Work Estimation using Conservation of Angular Momentum

The net rotor torque, which is the sum of incidence torque and torque due to flow turning, is calculated from the Euler work equation as the difference in angular momentum from the rotor inlet to the outlet, and the torque is multiplied by the rotor speed to get work rate or power. Because the velocity components and mass flux calculated using the computational model are non-dimensional, it is important to non-dimensionalize the torque in a similar manner. The contribution to the angular momentum flux, JF, for one channel over one cycle can be written as:

$$\mathrm{JF} = \mathrm{R}\,\mathrm{A_c} \int_0^{t_{cy}} \rho u c_t dt \tag{10}$$

Using reference density ρ^*, reference speed of sound a^*, channel axial length L and reference time $\frac{L}{a^*}$ to respectively non-dimensionalize density, velocity, channel radius and time in Eq. (10), the angular momentum flux can be written as:

$$\mathrm{JF} = \frac{2\pi R h}{N} \rho^* a^{*2} \left(\frac{L}{a^*}\right) L \int_0^{t_{cy}} R' \rho' u' c_t' dt' \tag{11}$$

where N is the number of channels in the rotor, R the channel mean radius, h is the channel height and L the channel length. The term inside the integral is the non-dimensional angular momentum flux through one port for a single channel over one cycle. The angular momentum flux can be expressed in terms of the non-dimensional flux, JF′:

$$\mathrm{JF} = \frac{2\pi R h}{N} \rho^* a^* L^2 \ \mathrm{JF}' \tag{12}$$

The net torque for all ports over n_{cy} cycles per revolution, τ, is the difference in angular momentum flux from the inlet to the outlet:

$$\tau = \left(\frac{N\mathrm{n_{cy}}}{t}\right)\frac{2\pi Rh}{N}\rho^* a^* L^2 \ [\mathrm{JF'(Port_{in})} - \mathrm{JF'(Port_{out})}] \tag{13}$$

Writing the time for one revolution of the rotor as $\frac{2\pi}{\Omega}$ and normalizing the rotational speed using L/a^* gives the final expression for the net torque:

$$\tau = Rh\rho^* {a^*}^2 L\Omega' \ [\mathrm{JF'(Port_{in})} - \mathrm{JF'(Port_{out})}]n_{cy} \tag{14}$$

The shaft power $\mathrm{P_{JF}}$ is the product of rotor torque and angular velocity:

$$\mathrm{P_{JF}} = R\ h\ \rho^* {a^*}^3 \Omega'^2 \ [\mathrm{JF'(Port_{in})} - \mathrm{JF'(Port_{out})}]n_{cy} \tag{15}$$

If the torque τ and rotational speed Ω are of opposite sign, work is transferred from the rotor to the gas similar to a compressor, and if they are of like sign, work is transferred from the gas to the rotor as in the case of a turbine.

2.3.2 Control Volume and Velocity Calculation

The work equation described in (15) requires calculation of tangential velocity components at the inlet and exit of the rotor. However, unlike traditional turbomachines, in the case of wave rotors a mean value for velocity cannot be used for calculating work because the flow inside the wave rotor is non-steady. The presence of ports creates internal pressure waves leading to non-uniform velocity at the inlet and exit. Therefore, the instantaneous rate of work is estimated as a function of angular

position of the channel and integrated across a cycle of rotation to calculate overall work transfer.

The flow work is estimated using a control volume approach with velocity triangles at the inlet and exit. The control volume, shown in Figure 6, encompasses the entire wave rotor and is assumed to have adiabatic walls with no external heat transfer in the present work. Velocity triangles are shown in

Figure 7 for general cases of positive and negative ζ that may occur at either end of the channel. In the velocity triangles, c is the velocity in the stationary frame of reference, w is the velocity in the channel frame of reference, c_t and w_t are the tangential component of velocity in the stationary and channel frame of reference, respectively, u is the axial component of velocity, and Ω and R are the rotational speed and channel mean radius of the rotor. The vector algebra of velocity triangles is applied at each end of the channel and for each computational time step as the channel completes one cycle of rotation. The duct angle β, blade angles ζ_r, ζ_l and rotational velocity ΩR are specified as design conditions. From the known conditions and the channel axial velocity distribution obtained at the end of simulation, the unknown velocity components in the velocity triangle can be calculated at each time step. When the flow is entering the channel (illustrated for the case of entry at the left end in Figure 7), the velocity components are calculated as follows:

$$c = \frac{u}{\cos(\beta)}$$
$$c_t = u\tan(\beta) \tag{16}$$

$$w_t = c_t - \Omega R$$

The angle i, the relative frame inflow angle previously defined in Eq. (9), must be equal to zero on average to avoid incidence loss. When the flow is leaving the channel (illustrated for the case of exit at the right end in Figure 7), the velocity components are calculated using:

$$w_t = u \tan(\zeta_r) \tag{17}$$

$$c_t = \Omega R + w_t$$

$$c = \sqrt{(u)^2 + (c_t)^2}$$

2.3.3 Shaft Work Estimation using Conservation of Energy

A numerical model must satisfy physical laws, be internally consistent, and ultimately validated through experiments. Many sub-models in the current model such as friction, heat transfer and mass leakage are based on empirical relationships calibrated from previous experimental research. Although these loss mechanisms are omitted in the current work, they will be needed in future efforts to provide the realism needed for experimental validation. The current model is passage-averaged to solve the governing equations in one dimension. Experimental testing is also needed to quantify the errors from this simplification in estimation of shaft work, mass flow rate, and other performance parameters. There are no reported experiments with non-axial wave rotors with details of boundary conditions to validate the present model. The present work includes a check of the internal consistency of shaft work calculation. In the

previous section, the shaft work was estimated using the principle of conservation of angular momentum. A second estimate of the shaft work can be obtained using conservation of energy. If the numerical model is developed correctly, the two approaches should agree.

The second approach for calculating the shaft power uses the enthalpy change and conservation of energy. The conservation of energy for an arbitrary control volume is:

$$\dot{Q} - \dot{W} = (\dot{m}h_o)_{out} - (\dot{m}h_o)_{in} \tag{18}$$

and assuming the control volume to be adiabatic and gas to have a constant specific hear, the equation can be rewritten as:

$$-\dot{W} = (\dot{m}h_o)_{out} - (\dot{m}h_o)_{in} \tag{19}$$

$$h_o = c_p T_e + \frac{c^2}{2}$$

The energy equation in (19) is non-dimensionalized in a manner similar to the torque equation. The work output for one channel over one cycle is given by:

$$-W = \left[\frac{2\pi Rh}{N} a^{*3} \rho^* \left(\frac{L}{a^*}\right)\left(\frac{1}{\gamma - 1}\right) \int_0^{t_{cy}} \rho' U' \left(T_e' + \frac{\gamma - 1}{2} c'^2\right) dt'\right] \tag{20}$$

The terms inside the integral can be written as the non-dimensional enthalpy flux, EF' which reduces Eq. (20) to :

$$-W = \frac{2\pi Rh}{N} a^{*2} \rho^* L \left(\frac{1}{\gamma - 1}\right) [EF'(\mathrm{Port}_{\mathrm{out}}) - EF'(\mathrm{Port}_{\mathrm{in}})] \quad (21)$$

The net shaft work output from conservation of energy for all the channels over one revolution is given by:

$$P_{EF} = R\, h\, \rho^*\, a^{*3}\, \Omega' \left(\frac{1}{\gamma - 1}\right) [EF'(Port_{out}) - EF'(Port_{in})] n_{cy} \quad (22)$$

The computation of angular momentum and stagnation enthalpy is made in the stationary, inertial frame of reference. The stagnation temperature is T with subscript *e* denotes temperature in stationary frame of reference. The power calculated from Eq. (15) and Eq. (22) should match if the numerical model is formulated and implemented correctly. The sign convention in Eq. (22) gives positive power if work is transferred from the gas to the rotor in the stationary frame of reference. The reference power used to convert from non-dimensional form to dimensional form is $R\, h\, \rho^* a^{*3}$ and is same in both the angular momentum formulation and conservation of energy formulation.

3. MODELING OF WAVE TURBINE OPERATING CYCLE

The extended model presented in Section 2 was used to simulate a three-port divider cycle wave rotor, a simple cycle that combines both compression and expansion and that has been studied extensively in prior work[14]. The model input parameters such as the pressure ratios, port opening and closing time and rotor speed were kept constant for all simulation and are given in Table 1. All loss mechanisms were neglected except the flow incidence loss, in order to isolate the contributions of the blade forces

to the overall work transfer. First, a three-port cycle with axial channels was simulated, and brief grid independence study was conducted. The flow incidence angle, and hence the incidence loss and torque, was then minimized in the axial configuration by changing the inlet duct angle. The optimal duct angle found in the axial case was then translated to the case with curved blades and the shaft power was estimated. The wave processes are also briefly described and analyzed in both the axial and non-axial channel cases.

Achieving a repeating identical 'limit' cycle solution is based on net zero mass accumulation over a cycle with no further change in the mass fluxes of ports. It is observed that constant port fluxes of mass usually ensures that fluxes of any other quantity like enthalpy and momentum becomes a constant over one cycle and the time-history of the cycle repeats exactly, making it periodic. A mass flux difference of 0.01% between inflow and outflow is used to check for a repeating cycle.

3.1 Effect of Computational Grid Size

To study the effect of grid density on the wave rotor gas dynamics, calculations were performed using both a low grid density (200 computational cells) and a high grid density (800 computational cells). The time steps for both cases were chosen to maintain a Courant number of 0.2. The mean channel pressure was calculated at every time step and is plotted for both grids in Figure 8. The difference in mean pressure for 200 and 800 computational cells is less than 1% indicating that the solution is highly grid independent. Further, the pressure at the middle of the channel is plotted in Figure 9 for both 200 and 800 computational cells. The mid-channel pressure for both grid densities

are within 1%, indicating that 200 computational cells are sufficient for the current work. Based on this brief grid study, 200 computational cells were used for the studies described in this section, with a non-dimensional computational cell size of 0.005 and a non-dimensional time step of 0.001, corresponding to a nominal Courant number of 0.2. In the case of non-reacting flow, only the contact interface needs to be resolved which can be done with 200 cells, but for wave rotors with reacting flow a higher grid density may be required to predict the speed and thickness of the flame front. It is noted that with shock-capturing numerical methods such as Roe's method, the accurate prediction of shock and pressure wave speeds has been accomplished with relatively coarse grids.

As the wave rotor rotates and the channel aligns itself with the ports, pressure waves are generated through instantaneous opening and closing of the ports. Choosing an appropriate computational time step is critical to accurately capture the waves. If the time step is too large then the waves are not captured accurately, but a time step that is too small will require unnecessarily high computational resources. In the current work, the time step used for the full cycle simulation of the wave rotor is 0.001 to maintain a nominal Courant number of 0.2, as stated above. To verify that this time step is sufficiently small to capture the waves, two simulations with shorter time steps were conducted with the same computational cell size of 0.005. The velocities at the inlet and outlet are plotted in Figure 10 and Figure 11, respectively, for three time steps: 0.0001, 0.0005 and 0.001. As expected, as the time step is decreased the temporal rise in pressure and velocity across any shock is sharper. However, as the time step is increased, the timing of travel is not noticeably changed. The code captures shocks and

predicts wave speeds consistently; for example, even the sharp expansion wave at the inlet end around 162° is essentially unchanged. Therefore, a time step of 0.001 is sufficient for the present simulations.

3.2 Three-Port Axial Channel Wave Rotor

The inlet duct needs to be designed to produce minimum possible incidence loss. In the simulation, the duct angle is an input parameter and can be varied to obtain the minimum incidence using a manual trial-and-error process. For an axial channel wave rotor, the only source of torque is through inflow incidence, as the outflow is axial and creates no torque, and therefore a duct angle designed to produce net zero incidence torque can be considered as the definition of the minimum incidence duct angle. The minimum incidence duct angle calculated for an axial channel serves as a starting point for minimizing incidence loss for the non-axial channel wave turbine.

To simulate an axial channel wave rotor using the wave turbine model, the blade angle was set to zero at both the inlet and outlet. The inlet duct angle was initialized at 0° and then increased in increments of 5° until the relative frame inflow angle i with respect to the channel reduced to zero, indicating minimum incidence loss. The shaft work associated with flow incidence in each channel is calculated as a function of its angular position over one cycle using both methods described in Section 2.3, and then integrated to get the overall torque and shaft power due to incidence mismatch for one cycle of rotation of the wave rotor. The shaft power is negative for small duct angles, indicating work being done on the gas by the rotor due to incidence. The shaft power

becomes less negative as the duct angle is increased and reaches zero for a particular duct angle, indicating that there is minimum incidence loss on average for the entire cycle. Further increasing the duct angle will result in positive shaft power where work is transferred from the gas to the rotor.

In the present case, the duct angle where the shaft power reduces to zero for the boundary conditions specified in Table 1 was found to be 38.1° as shown on Figure 12. The relative frame inflow angle, i, is also calculated from Eq. (16) as a function of angular position of the channel from inlet opening angle to inlet closing angle and is plotted in Figure 13 for every 10° change in duct angle. For a duct angle of 38.1°, the relative frame inflow angle is negative for the first half of the port open time and positive for the remaining half, providing 0° incidence on average at the design-point operating condition. This optimal duct angle is dependent on the operating conditions of the wave rotor, and thus a fixed duct angle will be optimal only at its design-point condition. A more sophisticated inlet system could include variable-angle inlet guide vanes and a control system to vary the duct angle based on the particular operating conditions.

To illustrate the predicted flow over one cycle of operation, an $x - t$ diagram of temperature and pressure within the channel and an axial velocity plot at the inlet and exit plane are shown in Figure 14. The non-dimensional axial velocity is indicated by a red dashed line for the right-side (outlet) ports and with a solid blue line for the left side (inlet) port. The low-pressure outflow port opens at 0° at the right end wall, initiating an expansion wave to accelerate and vent gas out through the port. The port then closes

at 51.5° generating a compression wave. The intermediate pressure inlet port opens at 108° and closes at 162° on the left end wall, where the propagation of shock wave pulls fresh gas into the rotor. The shock wave increases the pressure of the gas in the channel as it is pushed through the high-pressure port between 136.36° and 178.42° at the right end wall. At the close of the high-pressure port another shock wave is generated which undergoes multiple reflections at both left and right end walls. The shock and its multiple reflections increases the pressure as the channel aligns itself with the low pressure exhaust port. These gas dynamics throughout one cycle (from 0 to 360°) can be observed in the contour plot of temperature and pressure in Figure 14.

3.3 Three-Port Wave Turbine

In a wave rotor with non-axial blades, the shaft power or work rate transfer between the gas and the wave rotor has two components: work transfer from flow turning due to inlet incidence and work transfer due to angular momentum change through the length of the wave rotor channel. In an axial channel with no net flow turning, the only contributing component is from inlet incidence. As shown in the previous section, designing the inlet duct at an optimal angle can minimize inlet incidence and work transfer. For the case considered here (three-port cycle with operating conditions given in Table 1), the work rate of the axial-channel wave rotor reduces to zero at an inlet duct angle of 38.1°. A similar procedure must be followed for the non-axial channel case to find the duct angle that produces minimum incidence, i.e. the net torque due to incidence is zero. Using this optimum duct angle, the overall shaft

work calculated will be due only to the flow turning along the length of the curved channel.

Consider a wave turbine where the channels follow a parabolic blade profile with a left-end blade angle of ζ_l and a right-end blade angle of ζ_r, as illustrated in Figure 4. The values of ζ_r and ζ_l then uniquely determine the blade shape. Both values set to zero degrees will produce an axial channel. In the current work, one specific blade shape used is parabolic and symmetric and so the exit and inlet angles are equal with opposite sign, although the model can handle any complex blade shape. The optimal inlet duct angle calculated for the axial channel is used as an initial guess for the optimal duct angle for the non-axial (parabolic) channel. The duct angle is changed in small increments or decrements depending on a positive or negative inlet blade angle until the relative-frame inflow angle i matches the left-end blade angle ζ_l on average over the inlet port open time. The duct angles that minimize incidence for different inlet blade angles, ζ_l, for the particular pressure boundary condition in Table 1 were estimated and shown in Table 2. The relative frame inflow angle i with respect to channel direction and as a function of angular position of the channel for a +30° at the left to -30° at the right symmetric blade angle case is shown in Figure 15. Similar to the relative frame inflow angle for the axial channel case (Figure 13), the curved channel case also has a angle for the earlier part of the inlet port open time and positive angle for the later part, giving an average incidence of -0.12° over the entire inlet port open time. The incidence angle at the port opening and closing boundaries is often sharply

higher or lower because the axial velocity component becomes locally very small, resulting in sharply different velocity direction.

An $x - t$ plot of temperature, pressure and axial component of velocity for a symmetric +30° to -30° parabolic channel is shown in Figure 16. The port timing is identical to the timing in the axial channel case and the gas dynamics in terms of compression and expansion waves are similar to the axial channel. However, one noticeable difference is that the axial velocity component is lower for the non-axial channel compared to the axial channel. In the curved channel case, the tangential component of velocity contributes towards work transfer, which effectively causes a reduction in kinetic energy in the flow in the stationary frame-of-reference as it passes through the channels. In addition, the curvature of the blade increases the length of the channel and therefore the waves takes longer to travel the entire length of the channel.

The duct angle that minimizes incidence loss is calculated for the different blade angles using the methodology mentioned above. With the optimal duct angles listed in Table 2, pressure boundary condition in Table 1 and the corresponding blade angles, the effect of flow turning on shaft work is now analyzed. Since the blades are symmetric, as the inlet blade angle is varied from 0° to 30° an overall flow turning angle of 0° to 60° is obtained. The overall shaft power is estimated using the methods described in Section 2.3 for each of the blade angles and a plot of shaft power vs. blade angle is shown in Figure 17. The non-dimensional shaft work increases from 0 for the axial channel wave rotor to 0.16 for the 30° symmetric channel wave rotor. The positive sign indicates that work is being done by the gas on the rotor and the shaft power increases with blade

angle due to the increase in flow turning and angular momentum change from the inlet to the exit of the channel.

According to Eq. 16 and 23, the shaft power is normalized using $Rh\rho^* a^{*3}$. An experimental axial channel wave rotor[8] is used to obtain these reference conditions, with the expectation that this rig could be redesigned to accommodate a wave rotor with curved channels. In the experimental design, the mean radius R is 0.19 m, the passage height is 0.07 m, the reference speed of sound is $a^* = 338.40$ m/s and the reference density is $\rho^* = 1.22$ kg/m^3. Using the reference values, the dimensional shaft work for the 30° symmetric blade angle is found to be 100 kW or 135 hp. If we assume a turbomachine that expands flow from high pressure to low pressure, such that the pressure ratio is equal to the ratio between inlet port and low pressure port of the three-port wave rotor and works with the same mass flow rate then the turbomachine provides 210 kW. If we compare the wave rotor work with the turbomachine work, then the three-port wave turbine is capable of providing 52% of the turbomachine work. It should be noted that this power is calculated while neglecting heat transfer, frictional loses, leakage effects, finite port opening time and windage loses. Including these effects could lower the shaft work produced by flow turning inside the wave rotor. On the other hand, the port timings that were optimized for an axial channel may be suboptimal for the curved channel, and more optimal timing may improve the work output. These effects will be studied in future work.

4. CONCLUSION

A wave rotor is a device that uses non-steady but periodic flow in multiple channels or passages to generate internal pressure waves that can perform efficient energy transfer. In wave rotors with non-axial channels, the flow turning generates shaft work which can be used to power other devices in the system. Previous efforts on modeling the flow in a wave rotor resulted in development of a quasi-1d numerical model for wave rotors with axial channels. In the present work, this numerical model was extended to wave rotors with non-axial channels. First, the conservation equations were averaged over the channel cross-section using Favre averaging to develop quasi-1d transient flow equations for non-steady flow in slanted or curved channels. The resulting flow equations for curved channels have additional terms in the momentum and energy equations due to blade forces. These additional terms were allocated to the right side of the equation as quasi-source terms, preserving the form of the equations in the code originally developed for axial channels. The conservation equations were then solved using a Lax-Wendroff scheme and Roe's method of flux averaging to capture all flow discontinuities like shocks and expansion waves. The wave turbine model was validated using prior work for an expansion fan propagating through a non-axial channel and for an axial-channel wave rotor undergoing a three-port divider cycle.

Design of the inlet flow duct to produce minimum flow incidence into the channel is important to minimize incidence-related torque, which is a dissipative loss mechanism. Therefore, a model for losses due to inlet flow incidence was implemented in the extended wave rotor model and a procedure was developed for determining the

duct angle that minimizes incidence loss for a particular set of boundary and initial conditions. Finally, two methods for estimating the shaft work generated due to flow turning in a non-axial wave rotor were presented.

The extended model was then used to simulate a three-port divider wave rotor cycle with both axial and curved channels. The resulting transient flow field and wave patterns were analyzed using $x - t$ diagrams of temperature and pressure as well as plots of the flow velocity at the inlet and exit planes. The flow incidence torque was minimized by varying the inlet duct angle and the shaft power for the rotor was estimated for different blade angles. The shaft power was shown to increase with blade angle due to increase in flow turning and hence change in angular momentum. An initial estimate of dimensional shaft work for an experimental wave rotor with effective camber of $60°$ is predicted to be about 100 kW in the ideal scenario where all loss generating mechanisms such as heat transfer, friction, leakage and windage are absent. These effects will be studied during the next phase of work.

The model developed in the current work provides a foundation for the design of wave turbines for different engineering applications, including wave turbine combustors for power generation and aeropropulsion. Designing a wave turbine for experiments is challenging because the port and blade geometry must be designed very precisely to match the arrival of pressure waves. For a successful wave rotor experiment, port timing and duct angle selection are critical. Incorrect timing of the ports can result in reverse flow, and if the duct angle is not designed correctly, it can cause incidence loss at the inlet. Therefore, an accurate predictive numerical model is invaluable for efficient and

cost-effective design of wave turbines for experimental testing. The extended wave rotor model developed in the current work will next be used to explore the implications of different loss mechanisms to develop approaches for design optimization, a critical next step towards implementing wave turbines in real engineering applications.

References

[1] Akbari, P., Nalim, R., and Mueller, N., 2006, "A Review of Wave Rotor Technology and Its Applications," Journal of Engineering for Gas Turbines and Power, **128**(4), p. 717.

[2] Burghard, A., 1928, "Verfahren Zur Verdichtung von Gasen (Method for the Compression of Gases)."

[3] Meyer, A., 1947, "Recent Developments in Gas Turbines," Journal of Mechanical Engineering, **69**(4), pp. 273–277.

[4] Weber, H., 1995, *Shock Wave Engine Design*.

[5] Akbari, P., and Mueller, N., 2005, "Wave Rotor Research Program at Michigan State University," 41st AIAA/ASME/SAE/ASEE Joint Propulsion Conference and Exhibit.

[6] Mataczynski, M. R., Paxson, D. E., Polanka, M. D., and Hoke, J., 2016, "Experimental Performance of a Small Scale Pressure Wave Supercharger," *54th AIAA Aerospace Sciences Meeting*, American Institute of Aeronautics and Astronautics, Reston, Virginia.

[7] Mataczynski, M., Paxson, D. E., Hoke, J., and Schauer, F., 2017, "Design and Testing of a Small Pressure Wave Supercharger for an Industrial Diesel Engine," *55th AIAA Aerospace Sciences Meeting*, American Institute of Aeronautics and Astronautics, Reston, Virginia.

[8] Nalim, M. R., Snyder, P. H., and Kowalkowski, M., 2017, "Experimental Test, Model Validation, and Viability Assessment of a Wave-Rotor Constant-Volume Combustor," Journal of Propulsion and Power, **33**(1), pp. 163–175.

[9] Mathur, A., Shreeve, R. P., and Eidelman, S., 1984, "Numerical Techniques for Wave Rotor Cycle Analysis," American Society of Mechanical Engineers, Fluids Engineering Division (Publication) FED, Presented at the 1984 Winter Annual Meeting of the American Society of Mechanical Engineers, USA., **15**.

[10] Paxson, D. E., 1992, "A General Numerical Model for Wave Rotor Analysis," NASA STI/Recon Technical Report N 92 TM 31484.

[11] Paxson, D., 1998, "An Incidence Loss Model for Wave Rotors with Axially Aligned Passages," *34th AIAA/ASME/SAE/ASEE Joint Propulsion Conference and Exhibit*, American Institute of Aeronautics and Astronautics, Reston, Virigina.

[12] Welch, G. E., 1996, "Two-Dimensional Computational Model for Wave Rotor Flow Dynamics," ASME 1996 International Gas Turbine and Aeroengine Congress and Exhibition.

[13] Wilson, J., Welch, G., and Paxson, D., 2007, "Experimental Results of Performance Tests on a Four-Port Wave Rotor," *45th AIAA Aerospace Sciences Meeting and Exhibit*, American Institute of Aeronautics and Astronautics, Reston, Virigina.

[14] Wilson, J., 1998, "An Experimental Determination of Losses in a Three-Port Wave Rotor," Transactions-American Society of Mechanical Engineers Journal of Engineering For Gas Turbines And Power, **120**, pp. 833–842.

[15] Akbari, P., Nalim, R., Donovan, E. S., and Snyder, P. H., 2008, "Leakage Assessment of Pressure-Exchange Wave Rotors," *Journal of Propulsion and Power*, American Institute of Aeronautics and Astronautics, Reston, Virigina, pp.

732–740.
[16] Akbari, P., Nalim, R., and Snyder, P., 2006, "Numerical Simulation and Design of a Combustion Wave Rotor for Deflagrative and Detonative Propagation," *42nd AIAA/ASME/SAE/ASEE Joint Propulsion Conference and Exhibit*, American Institute of Aeronautics and Astronautics, Reston, Virigina.
[17] Elharis, T., Wijeyakulasuriya, S., and Nalim, M., 2011, "A Two-Step Reaction Model for Stratified-Charge Combustion in Wave-Rotors," *47th AIAA/ASME/SAE/ASEE Joint Propulsion Conference and Exhibit*, American Institute of Aeronautics and Astronautics, Reston, Virigina.
[18] Elharis, T., 2011, *A Multi-Step Reaction Model for Stratified Charge Combustion in Wave Rotors*, ProQuest Dissertations and Theses.
[19] Jagannath, R. R., Bane, S. P. M., and Nalim, M. R., 2015, "Wave Rotor Combustor Turbine Model Development," *51st AIAA/SAE/ASEE Joint Propulsion Conference*, American Institute of Aeronautics and Astronautics, Reston, Virginia.
[20] Karimi, A., and Nalim, M. R., 2016, "Ignition by Hot Transient Jets in Confined Mixtures of Gaseous Fuels and Air," Journal of Combustion, **2016**(9565839).
[21] Karimi, A., Rajagopal, M., and Nalim, M. R., 2014, "Traversing Hot-Jet Ignition in a Constant-Volume Combustor," Journal of Engineering for Gas Turbines and Power, **136**(4), p. 41506.
[22] Kilchyk, V., Nalim, M. R., and Merkle, C., 2013, "Scaling Interface Length Increase Rates in Richtmyer–Meshkov Instabilities," ASME Journal of Fluids Engineering, **135**(3), p. 31203.
[23] Matsutomi, Y., Meyer, S., Wijeyakulasuriya, S., Izzy, Z., Nalim, M., Shimo, M., Kowalkowski, M., and Snyder, P., 2010, "Experimental Investigation on the Wave Rotor Constant Volume Combustor," *46th AIAA/ASME/SAE/ASEE Joint Propulsion Conference and Exhibit*, American Institute of Aeronautics and Astronautics, Reston, Virigina.
[24] Nalim, M. R., 1999, "Assessment of Combustion Modes for Internal Combustion Wave Rotors," ASME Journal of Engineering for Gas Turbines and Power, **121**(2), pp. 265–271.
[25] Nalim, M. R., Li, H., and Akbari, P., 2009, "Air-Standard Aerothermodynamic Analysis of Gas Turbine Engines with Wave Rotor Combustion," ASME Journal of Engineering for Gas Turbines and Power, **131**(5), p. 54506.
[26] Nalim, M. R., 2000, "Longitudinally Stratified Combustion in Wave Rotors," Journal of Propulsion and Power, **16**(6), pp. 1060–1068.
[27] Nalim, M. R., 2002, "Thermodynamic Limits of Work and Pressure Gain in Combustion and Evaporation Processes," Journal of Propulsion and Power, **18**(6), pp. 1176–1182.
[28] Welch, G. E., and Larosiliere, L., 1997, "Passage-Averaged Description of Wave Rotor Flow," *33rd Joint Propulsion Conference and Exhibit*, American Institute of Aeronautics and Astronautics, Reston, Virigina.
[29] Welch, G. E., and Paxson, D. E., 1998, "Wave Turbine Analysis Tool Development," *34th AIAA/ASME/SAE/ASEE Joint Propulsion Conference and Exhibit*, American Institute of Aeronautics and Astronautics, Reston, Virigina.
[30] Larosiliere, L. M., 1995, "Wave Rotor Charging Process - Effects of Gradual Opening and Rotation," Journal of Propulsion and Power, **11**(1), pp. 178–184.

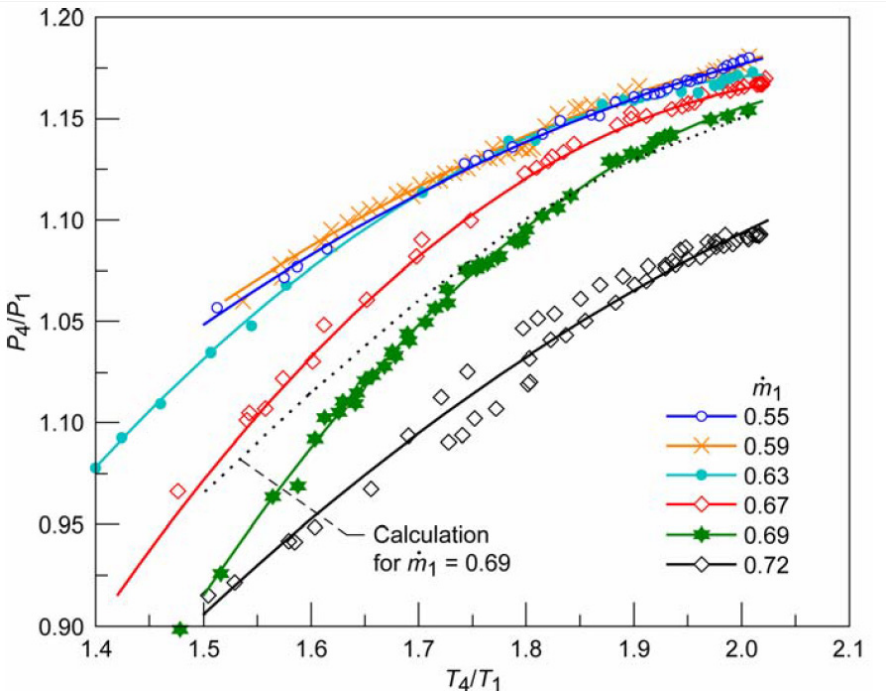

Figure 1 : Experimental measurements and computational predictions of pressure ratio for a four-port wave rotor[13]

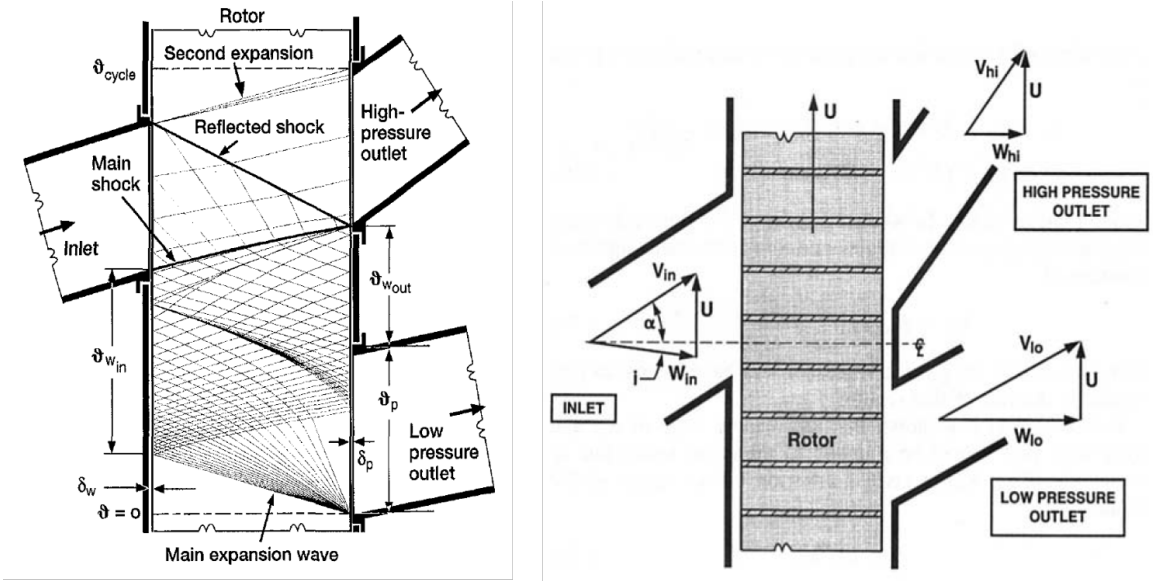

Figure 2 : Unwrapped view of the three-port wave rotor with internal waves and velocity diagrams[14]

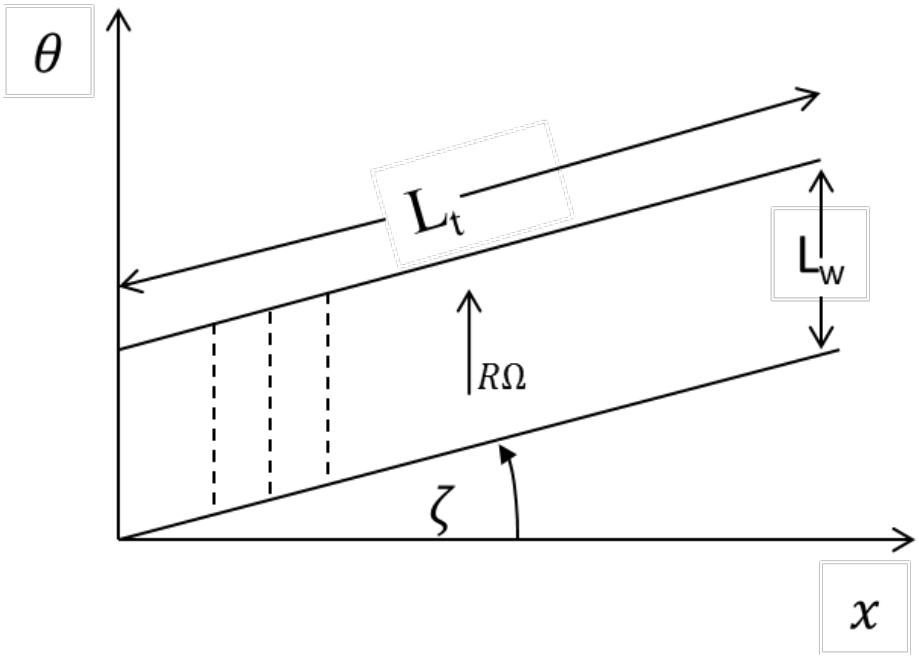

Figure 3: Schematic of a slanted or “staggered” straight wave rotor channel

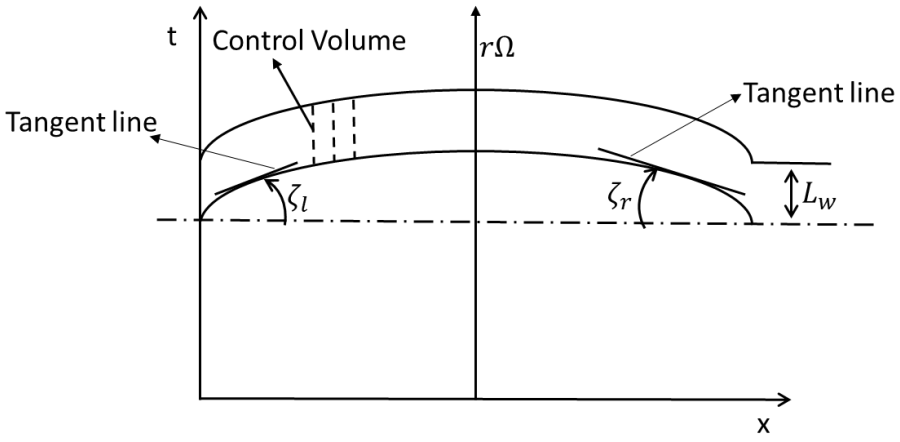

Figure 4: Schematic of a "non-staggered" symmetrically curved wave rotor channel

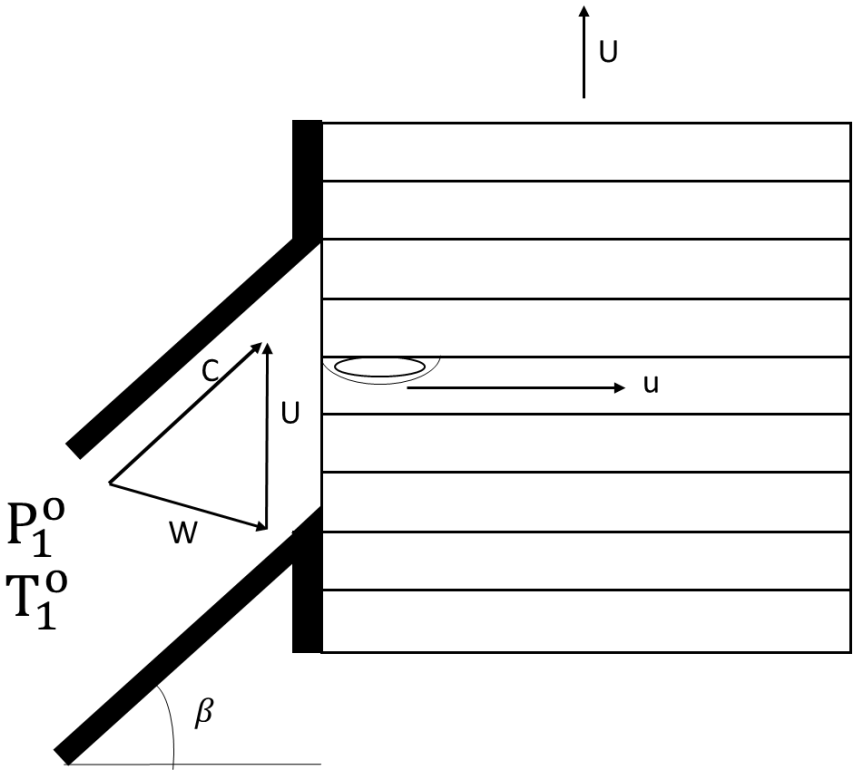

Figure 5 : Schematic illustrating the relative frame inflow angle of the flow at the wave rotor inlet [11]

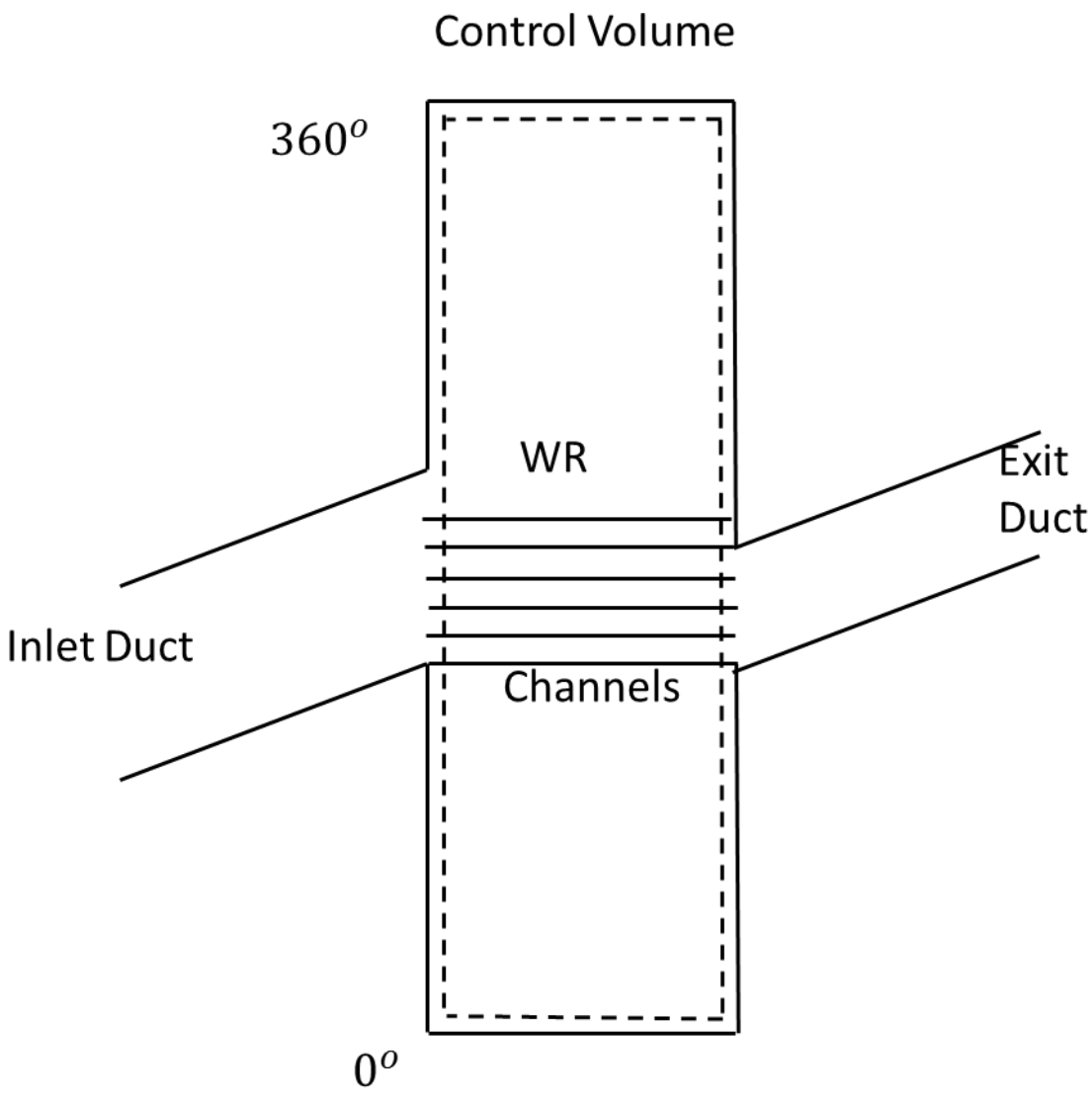

Figure 6 : Control volume used for estimating work output for the wave rotor and the channel geometry

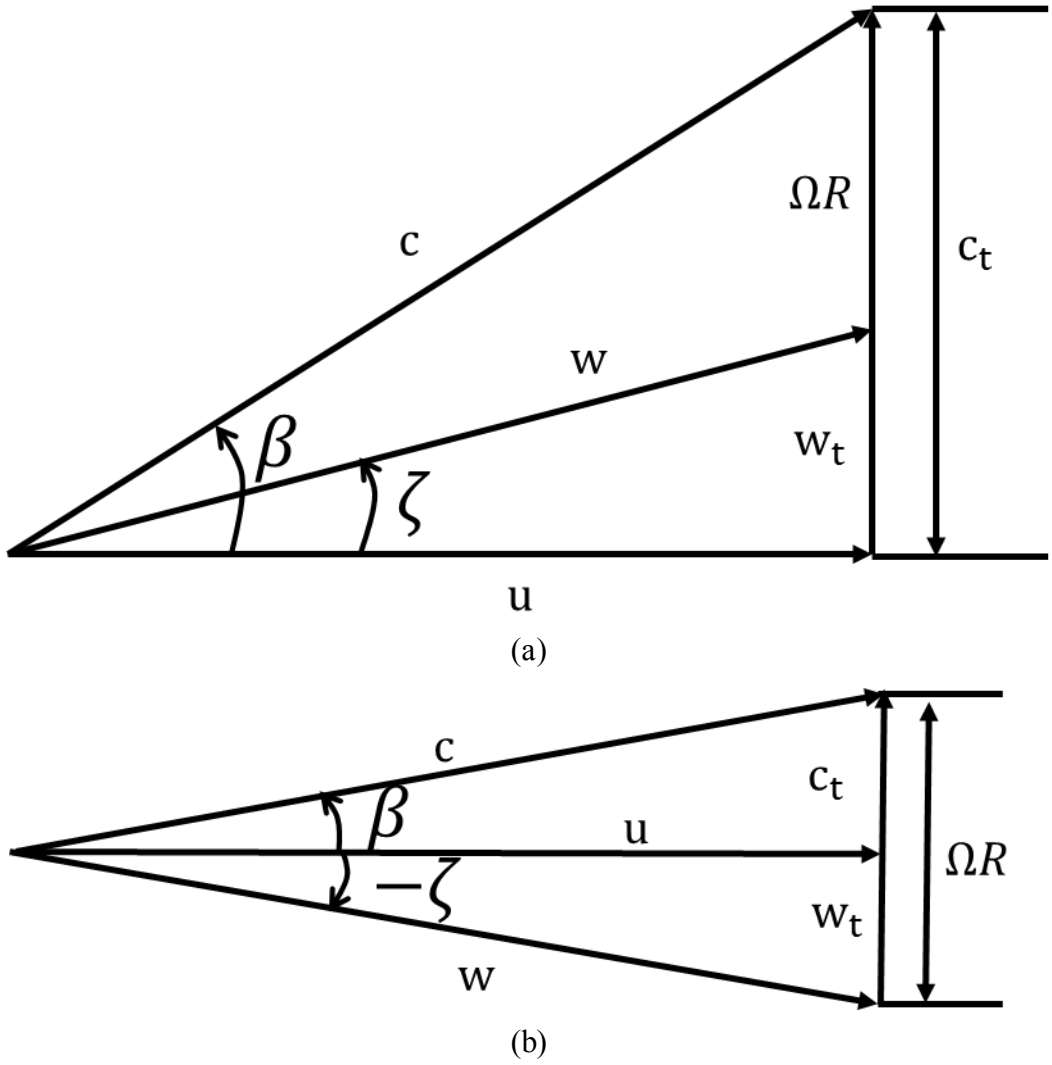

Figure 7 : Velocity triangles for (a) positive and (b) negative blade angle

Table 1: Three-Port Divider Cycle Parameters for Axial and Non-Axial Channel Cases

Parameter	Value (Non-Dimensional)
High Pressure Ratio	1.8
Low Pressure Ratio	0.7
Channel Opening Time	0
Inlet Blade Angle	0
Exit Blade Angle	0
Inlet Port Opening Time	1.89
Inlet Port Closing Time	2.83
High Pressure Port Opening Time	2.38
High Pressure Port Closing Time	3.11
Low Pressure Port Opening Time	0
Low Pressure Port Closing Time	0.9
Rotor Speed	0.5
Radius	1

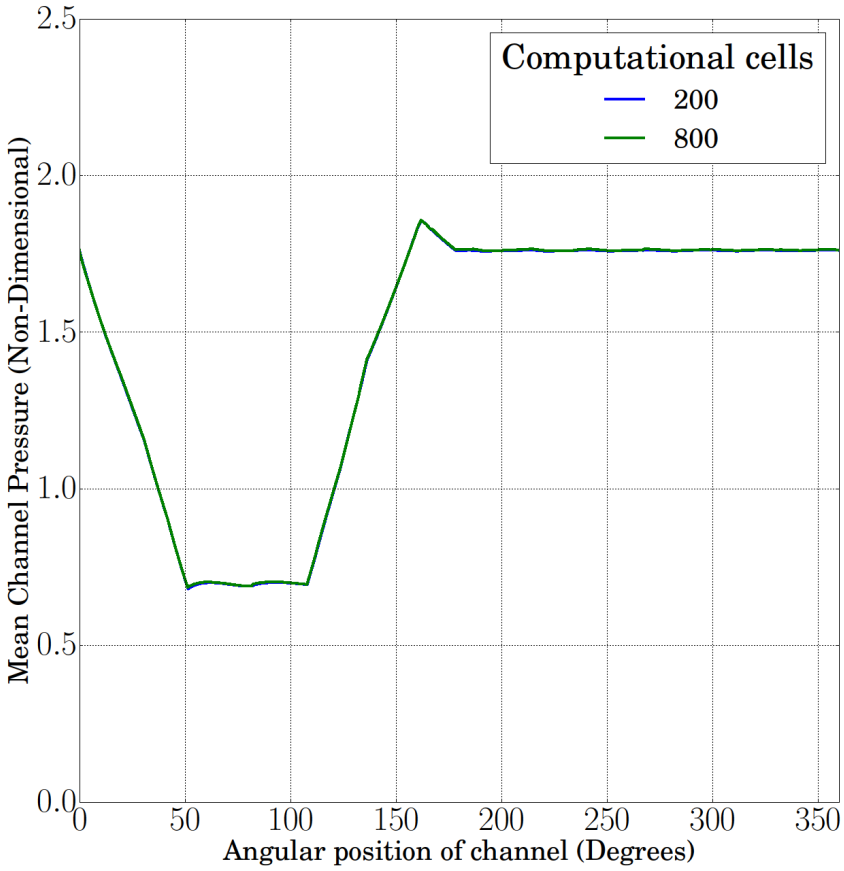

Figure 8 : Mean channel pressure as a function of angular position of channel for different grid densities

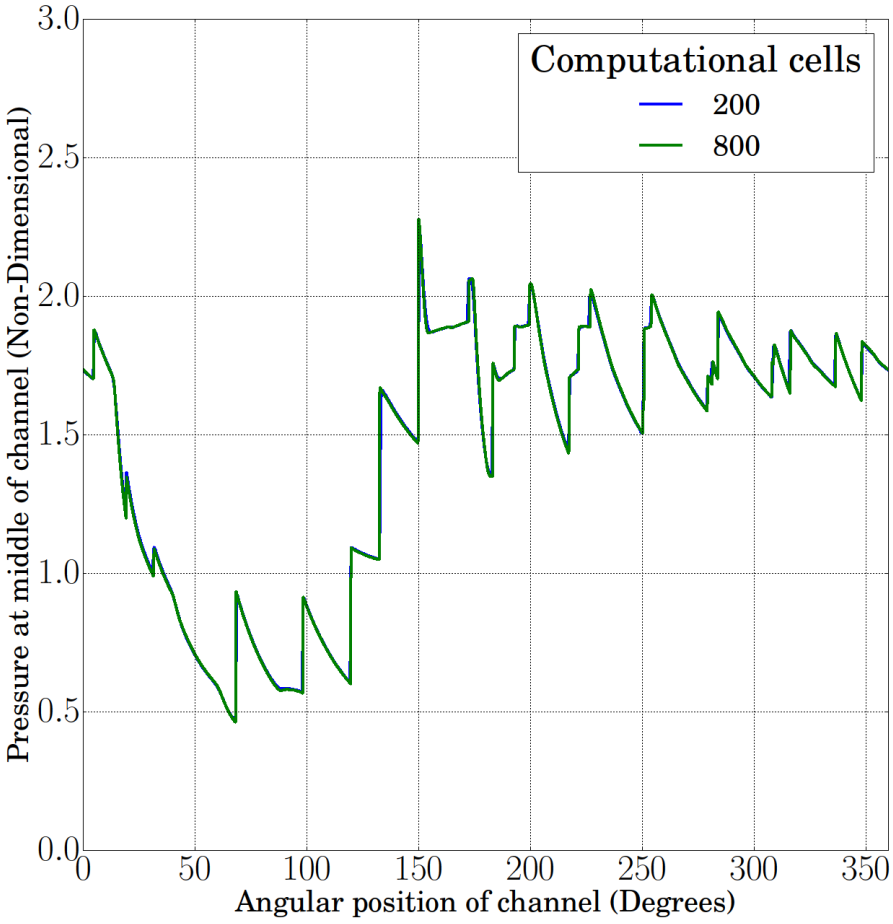

Figure 9 : Pressure at middle of the channel as a function of angular position of channel at different grid densities

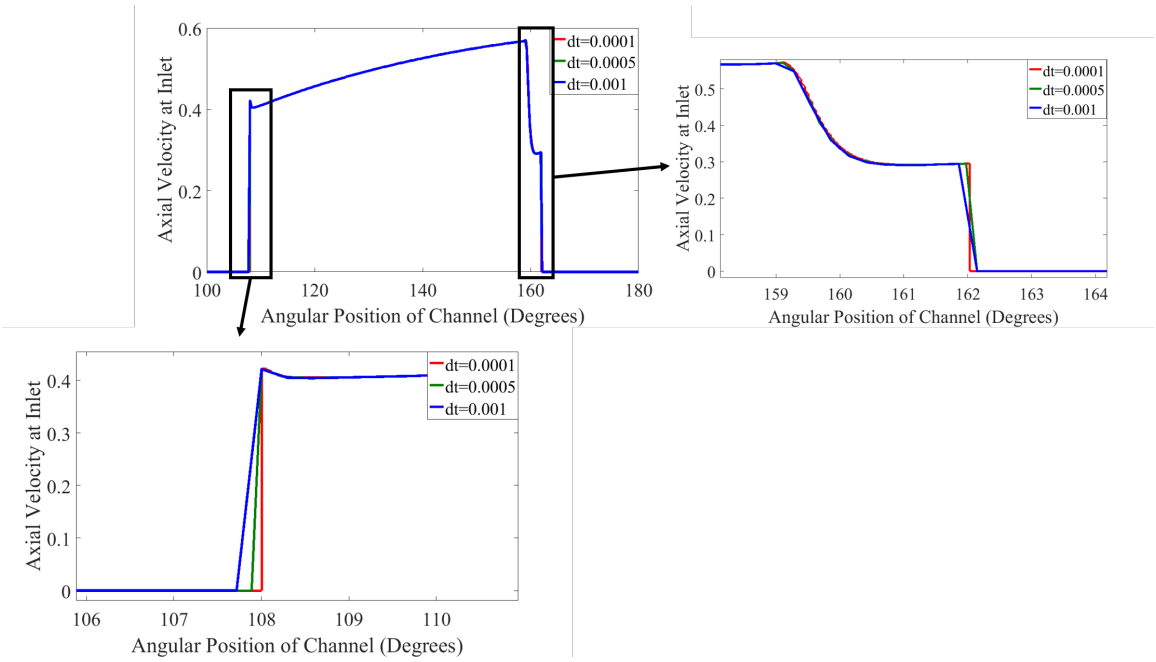

Figure 10 : Velocity at inlet for three computational time steps. Zoomed-in view shows the shock wave timing at 108° and expansion wave profile at 159-162°

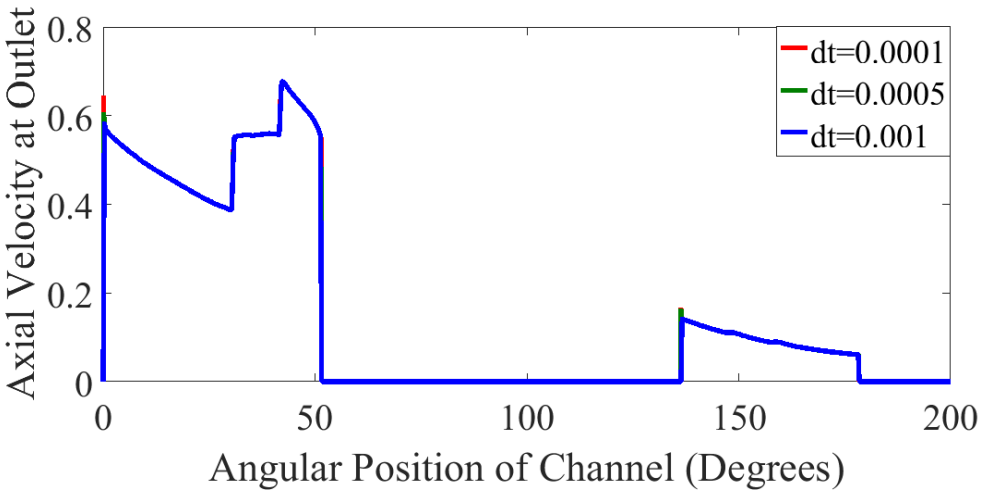

Figure 11 : Velocity at the outlet for three computational time steps.

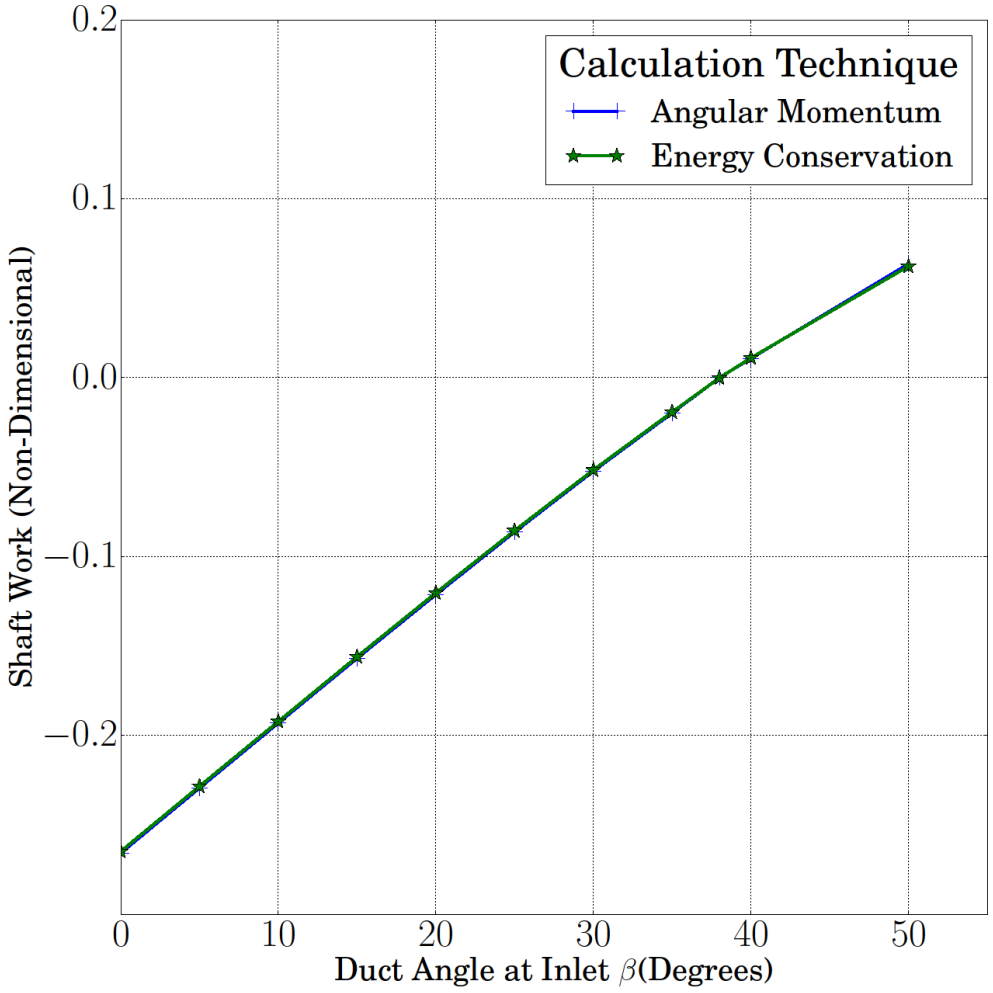

Figure 12 : Shaft power due to incidence mismatch for an axial channel

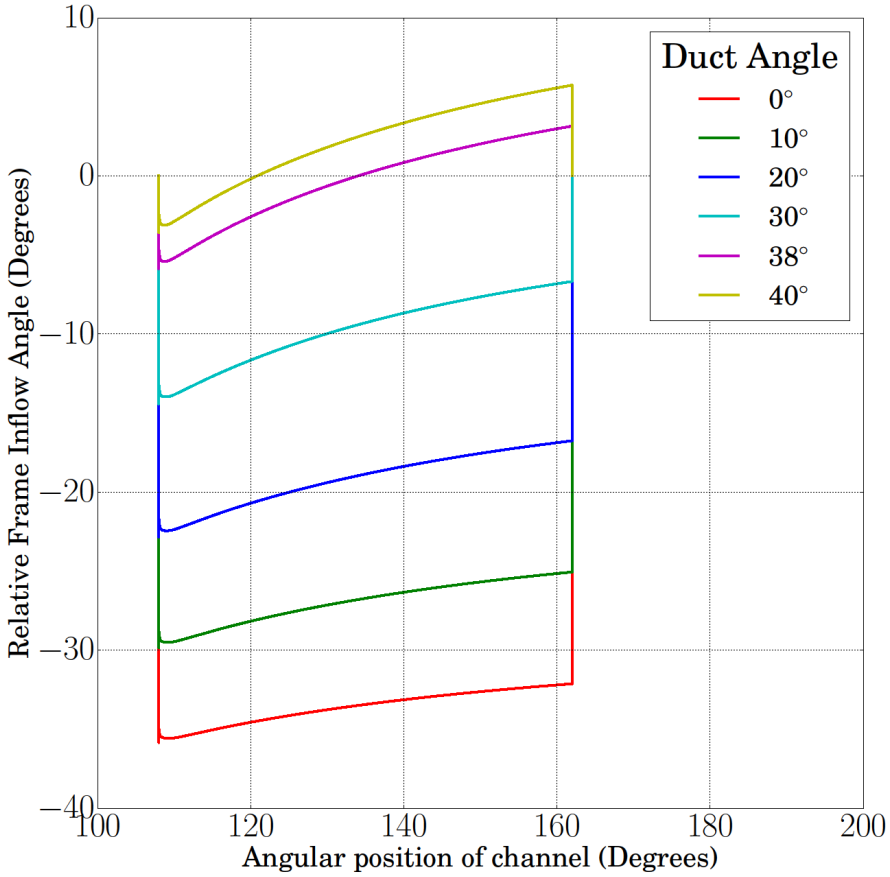

Figure 13: Relative frame inflow angle as a function of angular position of the channel for an axial-channel three-port wave rotor

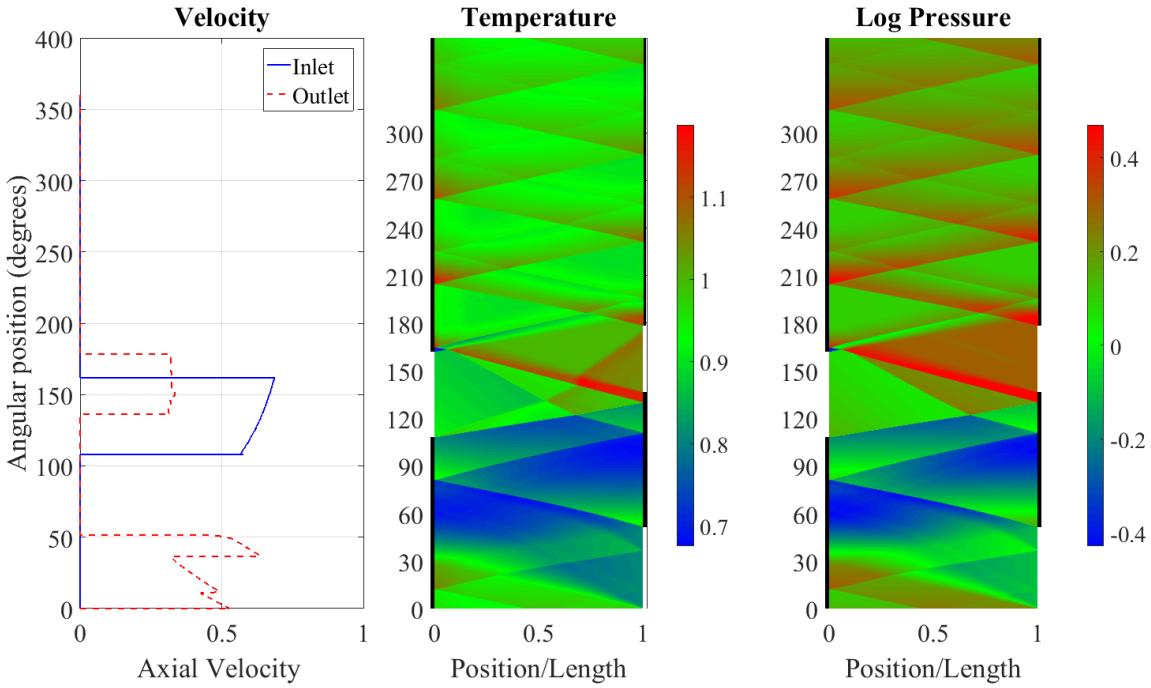

Figure 14: Axial velocity, temperature and the logarithm of pressure for an axial-channel three-port wave rotor with optimal duct angle

Table 2: Optimal Inlet Duct angle for the different inlet end blade angle, ζ_l

Inlet End Blade Angle (Degrees)	Duct Angle (Degrees)
0	38.1
5	43.1
10	46.4
15	48.7
20	51.6
25	55.4
30	58.4

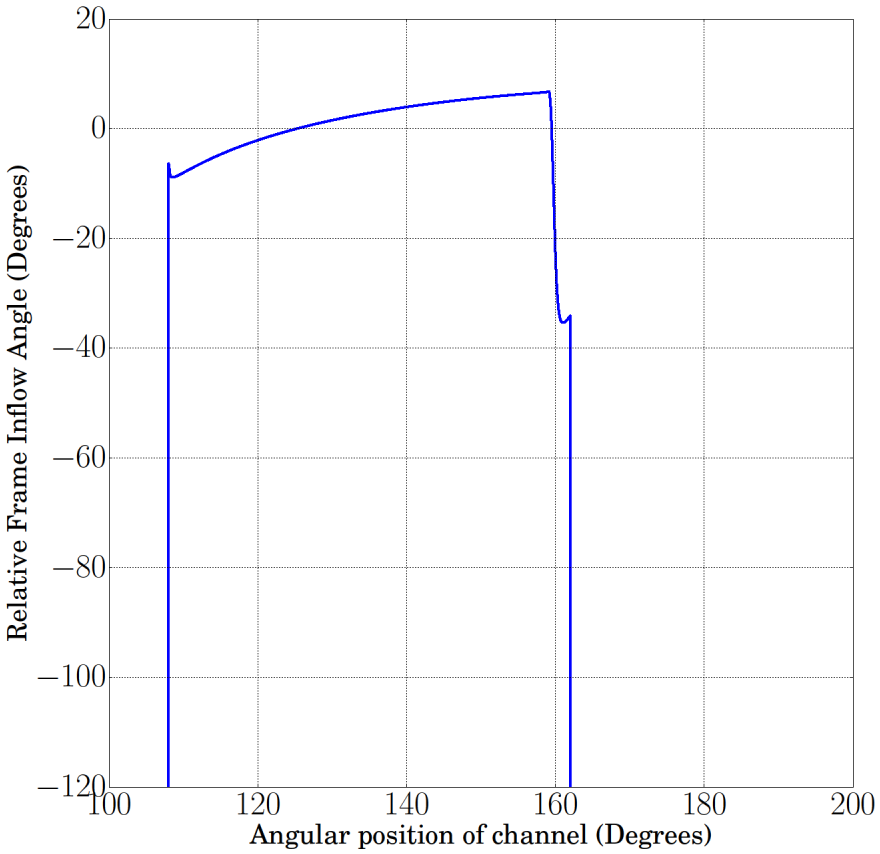

Figure 15: Relative frame inflow angle with respect to channel inlet angle for +30° to -30° symmetric blade wave turbine

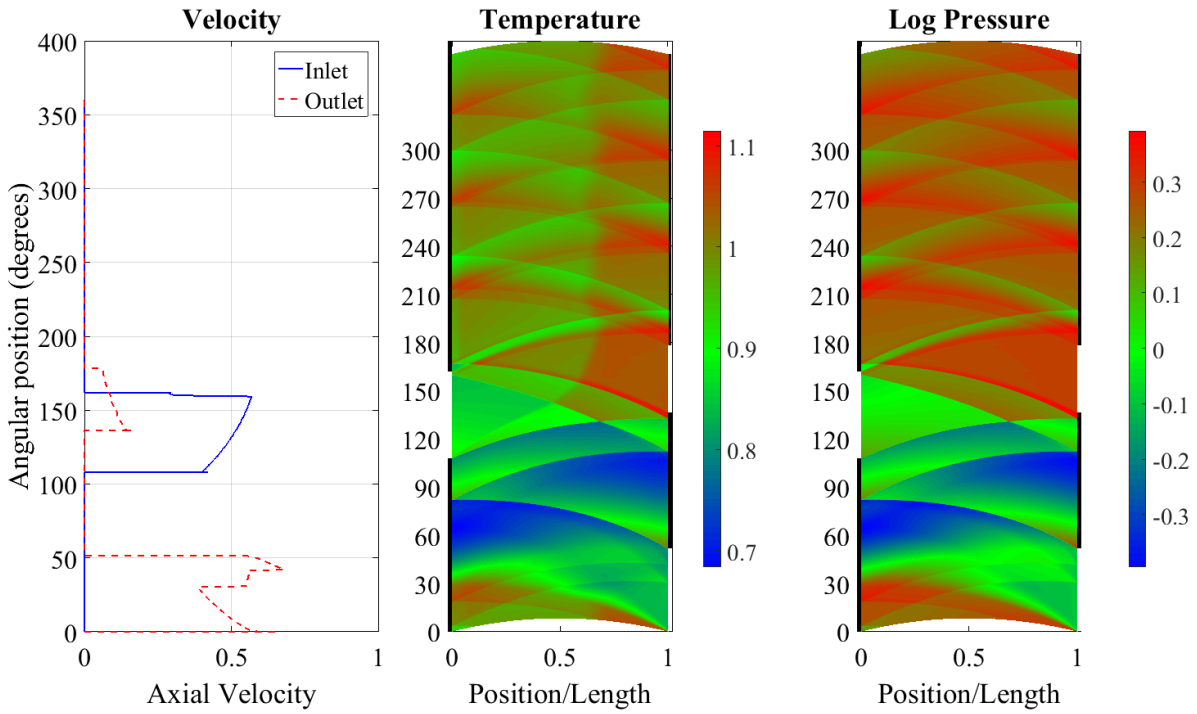

Figure 16: Axial velocity, Temperature and Log of Pressure (all non-dimensional) for three-port wave turbine with +30° to -30° symmetric parabolic blade and optimal duct angle

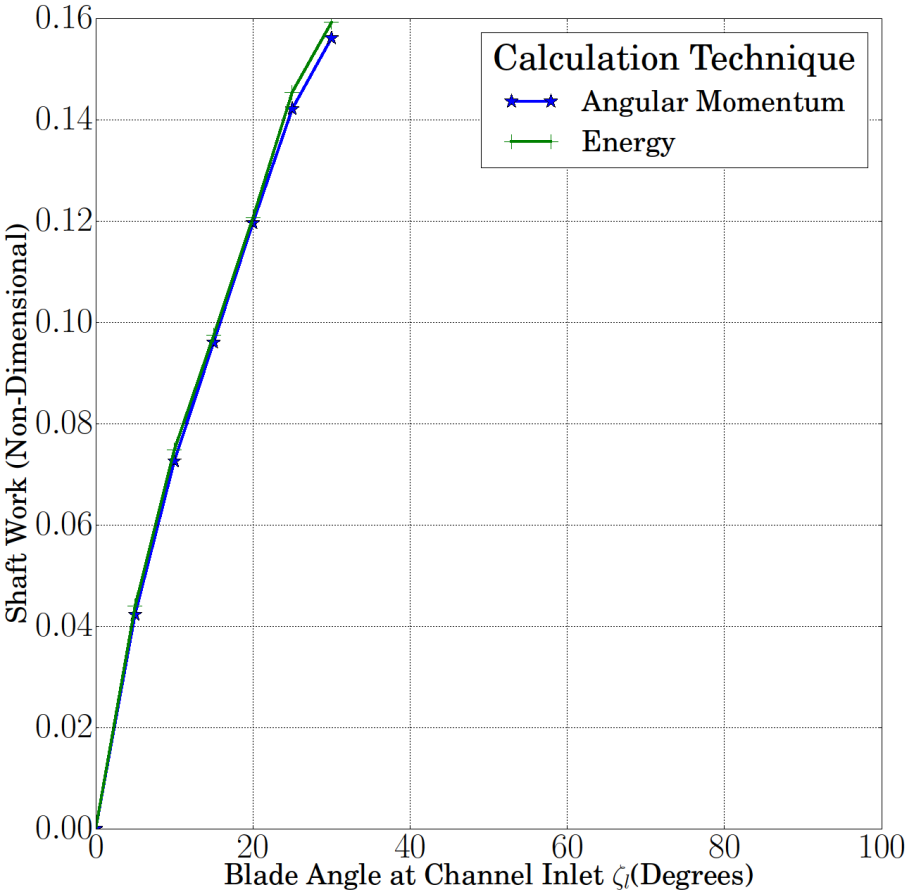

Figure 17 : Shaft power due to flow turning in a wave turbine with symmetric blades

NOMENCLATURE

$\dot{m}$	Mass flow rate
ρ	Density
$\vec{u}$	Velocity
F_B	Blade force
F_c	Momentum correlation source terms
Q_c	Passage averaged effective heat flux term
h_I	Local specific rothalpy
R	Radius of the rotor
Ω	Angular speed
p	Pressure
T	Temperature
C_p	Specific heat at constant pressure
δ	Blade angle factor
A_c	Channel area
χ	Source vector due to blade forces
ψ	Source vector due to leakage, friction and heat transfer

Φ	Meridional flow angle
ζ	Blade angle
β	Duct angle
i	Relative frame inflow angle
γ	Specific heat ratio
τ	Torque
P	Shaft power
$=$	Density weighted passage average
$\_$	Unweighted passage average
Δ_θ	Pitchwise difference
Δ_r	Spanwise difference
$'$	Prime superscript indicates non-dimensional variable
$*$	Star superscript indicates reference state conditions

Subscripts

x	Axial component
t	Tangential component
r	Right side of the rotor
l	Left side of the rotor
JF	Angular Momentum Flux

EF	Enthalpy Flux
p	Rotor passage leading blade surface
s	Rotor passage trailing blade surface

Figure Captions List

Fig. 1 Experimental measurements and computational predictions of pressure ratio for a four-port wave rotor[13]

Fig. 2 Unwrapped view of the three-port wave rotor with internal waves and velocity diagrams[14]

Fig. 3 Schematic of a slanted or "staggered" straight wave rotor channel

Fig. 4 Schematic of a "non-staggered" symmetrically curved wave rotor channel

Fig. 5 Schematic illustrating the relative frame inflow angle of the flow at the wave rotor inlet [11]

Fig. 6 Control volume used for estimating work output for the wave rotor and the channel geometry

Fig. 7 Velocity triangles for (a) positive and (b) negative blade angle

Fig. 8 Mean channel pressure as a function of angular position of channel for different grid densities

Fig. 9 Pressure at middle of the channel as a function of angular position of channel at different grid densities

Fig. 10 Velocity at inlet for three computational time steps. Zoomed-in view shows the shock wave timing at 108° and expansion wave profile at 159-162°

Fig. 11 Velocity at the outlet for three computational time steps.

Fig. 12 Shaft power due to incidence mismatch for an axial channel

Fig. 13 Relative frame inflow angle as a function of angular position of the channel for an axial channel three port wave rotor

Fig. 14 Axial velocity, Temperature and Log Pressure for an axial channel three port wave rotor with optimal duct angle

Fig. 15 Relative frame inflow angle with respect to channel inlet angle for +30° to -30° symmetric blade wave turbine

Fig. 16 Axial velocity, Temperature and Log of Pressure (all non-dimensional) for three-port wave turbine with +30° to -30° symmetric parabolic blade and optimal duct angle

Fig. 17 Shaft power due to flow turning in a wave turbine with symmetric blades

Table Caption List

Table 1 Three-Port Divider Cycle Parameters for Axial and Non-Axial Channel Cases

Table 2 Optimal Inlet Duct angle for the different inlet end blade angle, ζ_l